Ice flow sensitivity to geothermal heat flux of Pine Island Glacier, Antarctica

E. Larour,[1] M. Morlighem,[2] H. Seroussi,[1] J. Schiermeier,[1] and E. Rignot[1,2]

Received 9 February 2012; revised 20 September 2012; accepted 27 September 2012; published 16 November 2012.

[1] Model projections of ice flow in a changing climate are dependent on model inputs such as surface elevation, bedrock position or surface temperatures, among others. Of all these inputs, geothermal heat flux is the one for which uncertainty is greatest. In the area of Pine Island Glacier, Antarctica, available data sets differ by up to a factor of 2.5. Here, we evaluate the impact of such uncertainty on ice flow, using sampling analyses based on the Latin-Hypercube method. First, we quantify the impact of geothermal heat flux errors on ice hardness, a thermal parameter that critically controls the magnitude of ice flow. Second, we quantify the impact of the same errors on mass balance, specifically on the mass flux advecting through thirteen fluxgates distributed across Pine Island Glacier. We contrast our results with similar uncertainties generated by errors in the specification of ice thickness. Model outputs indicate that geothermal heat flux errors yield uncertainties on ice hardness on the order of 5–7%, with maximum uncertainty reaching 15%. Resulting uncertainties in mass balance remain however below 1%. We discuss the uncertainty distribution and its relationship to the amount of heat available at the base of the ice sheet from friction, viscous and geothermal heating. We also show that comparatively, errors in ice thickness contribute more to model uncertainty than errors in geothermal heat flux, especially for fast-flowing ice streams.

Citation: Larour, E., M. Morlighem, H. Seroussi, J. Schiermeier, and E. Rignot (2012), Ice flow sensitivity to geothermal heat flux of Pine Island Glacier, Antarctica, *J. Geophys. Res.*, *117*, F04023, doi:10.1029/2012JF002371.

1. Introduction

[2] Ice flow models used to project the mass balance of Antarctica and Greenland on decadal timescales are limited by uncertainties in model inputs. Such inputs include the ice sheet geometry (surface elevation, bedrock position or ice thickness, and grounding-line position) and boundary conditions (geothermal heat flux and basal drag at the ice/bed interface as well as temperature at the surface). Traditionally, the view was that ice thickness and surface elevation are critical because of their role in the stress-balance equations [*MacAyeal*, 1989; *Blatter*, 1995; *Pattyn*, 2003]. However, some model inputs, such as geothermal heat flux at the base of the ice sheet are so ill-constrained as to justify the need to assess the impact such lack of knowledge might have on model outputs.

[3] To specify geothermal heat flux in Antarctica, modelers rely on several data sets, among them: 1) the data set by *Shapiro and Ritzwoller* [2004], inferred using a global seismic model and 2) the data set by *Maule et al.* [2005], generated using satellite magnetic data. In the first data set, uncertainty is high, with a standard deviation ranging from 20 mW/m^2 in East-Antarctica to 90 mW/m^2 in West-Antarctica, particularly in the area of Pine Island Glacier (Figure 1). In some areas, the uncertainty is as high as the value of the geothermal heat flux itself. The second data set by *Maule et al.* [2005] is consistently lower across Antarctica, with relative differences to *Shapiro and Ritzwoller* [2004] ranging from 30% to 140%.

[4] Other types of data sets have also been used, especially for long reconstructions of ice flow, such as in *Ritz et al.* [1997, 2001], *Kerr and Huybrechts* [1999], *Hansen and Greve* [1996], *Takeda et al.* [2002], or *Pollard et al.* [2005]. In these simulations however, geothermal heat flux is spatially uniform over long distances. In Antarctica, it ranges between 42 and 60 mW/m^2 in *Ritz et al.* [1997], 42 and 105 mW/m^2 in *Hansen and Greve* [1996], and 54.6 mW/m^2 (for the East Antarctic Ice Sheet, EAIS) and 65 mW/m^2 (for the West Antarctic Ice Sheet, WAIS) in *Kerr and Huybrechts* [1999]. For million-year paleo-reconstructions, *Pollard et al.* [2005] used among others a data set ranging from 55 mW/m^2 in the EAIS (except West of Victoria Land, where values reached 41 mW/m^2) to 60 mW/m^2 in the Trans-Antarctic mountains and 70 mW/m^2 in the WAIS. For almost all of the studies cited, one of the common findings was that geothermal heat flux does not have a strong influence on global ice sheet volume and extent, but rather on the pattern of basal melting rate.

[1]Jet Propulsion Laboratory, California Institute of Technology, Pasadena, California, USA.
[2]Department of Earth System Science, University of California, Irvine, California, USA.

Corresponding author: E. Larour, Jet Propulsion Laboratory, California Institute of Technology, 4800 Oak Grove Dr., Pasadena, CA 91109-8099, USA. (eric.larour@jpl.nasa.gov)

0148-0227/12/2012JF002371

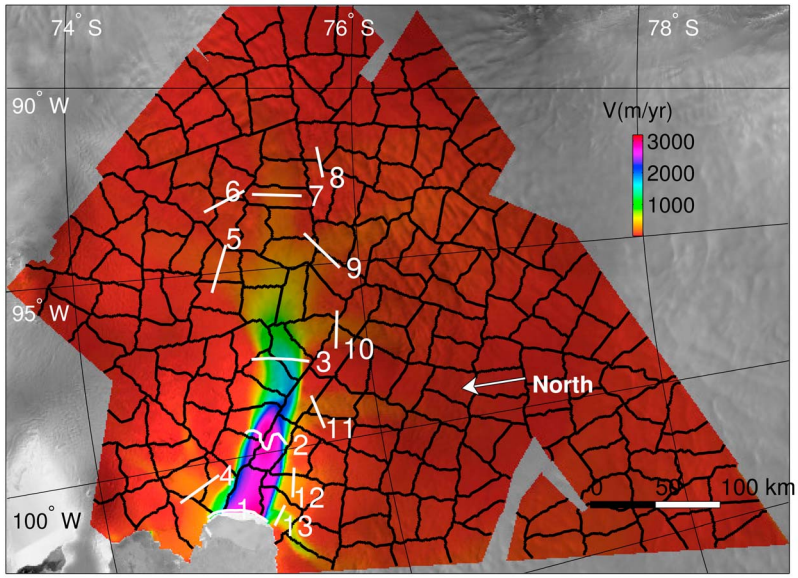

Figure 1. Fluxgates used to compute mass fluxes on tributaries of PIG. Each gate is numbered from 1 to 13, and corresponds to one tributary. Gate 1 coincides with the ice front, and gate 2 coincides with the 1996 grounding line [*Rignot*, 2008a]. The gates are superimposed on an InSAR surface velocity magnitude map of the area [*Rignot*, 2008a]. Sampling analyses are carried out on this glacier, based on partitioning of the mesh into 200 equal area partitions, plotted in black.

[5] On shorter timescales however (decadal to centennial), very few studies have attempted to quantify the exact impact of uncertainty in geothermal heat flux on the mass balance of fast-flowing ice streams. In addition, the lack of spatial variability exhibited by such data sets as *Ritz et al.* [1997, 2001], *Kerr and Huybrechts* [1999], *Hansen and Greve* [1996], *Takeda et al.* [2002], and *Pollard et al.* [2005], is not adapted to sensitivity studies at the local level. Parameter space studies have of course been carried out such as in *Ritz et al.* [1997, 2001], *Kerr and Huybrechts* [1999], and *Hansen and Greve* [1996], but these studies were based on simplified ice flow models running at coarse resolution. In particular, these studies focused on the impact on ice volume and extent of the entire ice sheet, not on how mass balance is affected at the local level. *Heimbach and Bugnion* [2009] were indeed the first ones to assess short-term local variations in the mass balance of a large ice sheet in response to variations in basal friction and surface accumulation. The approach relied on adjoint-based methods to assess sensitivities, using the SImulation COde for POLythermal Ice Sheets, SICOPOLIS [*Greve*, 1997a, 1997b]. For more details on the adjoint-based method, we refer the reader to *Giering and Kaminski* [1998], *Utke et al.* [2008], and *Hascoët* [2004]. Their approach revealed sensitivities at the local level that exhibited positive feedback when least expected. For example, in some areas, decreasing basal friction resulted in increases in ice sheet volume instead of thinning, as would be expected. This reinforced the argument that further analyses of how variations in model inputs affect local ice flow dynamics were indeed necessary.

[6] In *Larour et al.* [2012a], a systematic analysis of the sensitivity of Pine Island Glacier's mass balance (PIG) was carried out with respect to uncertainties in ice thickness, basal friction, and ice hardness. PIG was chosen because of its importance in controlling the dynamics of the WAIS, and because it is representative of fast-flowing ice streams, which are most susceptible to evolve in the next decades to centuries. The goal of the study was to assess the influence of each key parameter independently, in order to quantify error margins on key diagnostics such as mass flux across the entire ice stream. From measurements, only uncertainties in ice thickness were available. For basal friction and ice hardness, arbitrary estimates were made in the level of prescribed uncertainty (5%), which reduced the impact of the sensitivity analysis to a simple comparison between equally constrained uncertainties in three model inputs: ice thickness, basal friction and ice hardness.

[7] The reason uncertainty in basal friction was unknown is because basal friction is usually the product of a model inversion [*MacAyeal*, 1993], which is computationally difficult to sample for uncertainties. Short of an inversion, basal friction would need to be modeled, relying on an underlying hydrological model to link water pressure to basal drag [*Johnson*, 2002; *Le Brocq et al.*, 2009]. Such a model is currently a work in progress, and is outside of the scope of the present study. On the other hand, there is no reason why ice hardness uncertainty cannot be inferred from a coupled thermomechanical model such as ISSM [*Larour et al.*, 2012b]. In such a thermomechanical model, uncertainties in geothermal heat flux will propagate forward and impact the ice hardness, one of the main outputs of the thermal component, which in turn will impact mass balance, one of the main outputs of the mechanical component. Our goal here is to use the data sets that best capture the variability in geothermal heat flux, namely the *Shapiro and Ritzwoller* [2004] and *Maule et al.* [2005] data sets, and use them to constrain a sampling analysis of a fast-flow capable thermomechanical model to significantly improve on *Larour*

et al. [2012a]. The objectives are: 1) to quantify the uncertainty in ice hardness arising from variations in geothermal heat flux propagated forward through a thermal model of PIG; and 2) to quantify the resulting uncertainty in mass balance propagated forward through a mechanical model. In order to assess the mass balance of PIG, we rely on the value of the mass flux at each of thirteen fluxgates evenly distributed across PIG (see Figure 1).

[8] In the first part of the study, we describe the model used to capture the thermal and mechanical regime of the ice flow as well as the state of basal friction as inverted using InSAR surface velocities, and the sampling methods used to compute uncertainties. In the second part, we describe the model setup, including data sets, meshing strategies and computational considerations. In the third part, we present the results of our sampling analyses, first for the thermal regime, and second for the mechanical ice flow model. In the fourth part, we discuss the results and their implications in terms of PIG's mass balance and how well models are able to capture it. We finish by concluding on the relevance of this type of sampling studies and its impact on improving projections of mass balance in Antarctica, and the contribution to sea level rise in a changing climate.

2. Model

[9] PIG is a fast-flowing ice stream for which surface velocities can reach up to 4,500 m/yr [*Rignot*, 2008a; *Joughin et al.*, 2010]. This ice stream exhibits intense sliding at the ice/bed interface, with almost negligible vertical shearing through the entire thickness. This type of ice flow regime is well modeled using the two-dimensional (2D) Shelfy-Stream Approximation (SSA) [*MacAyeal*, 1989]. Horizontal components of the velocity are assumed to be constant through the ice thickness, and the vertical velocity component is recovered through the incompressibility equation. Both horizontal and vertical models are decoupled, because we neglect bridging effects (see *van der Veen and Whillans* [1989], *Pattyn* [2003], and *Morlighem et al.* [2010] for more details), which ensures the system of equations is computationally efficient. For more details on our implementation of these equations, we refer the reader to *Larour et al.* [2012b]. The limits of SSA appear in the upper part of the ice stream, where vertical shearing is more intense, and higher-order ice flow models become necessary [*Pattyn*, 1996], as well as near the grounding line, where increasing bridging effects become important, requiring the use of full-Stokes models [*Morlighem et al.*, 2010].

[10] It can be argued that the thermal regime will not strongly depend on higher-order stress representations, but more on the amount of viscous and frictional heating captured by the mechanical model and used as source terms for the thermal model. Therefore, sampling analyses based on this type of ice flow model are probably necessary. For the mass balance of PIG, the question may be asked whether a SSA approach is warranted, outside of computational considerations, which obviously favor the SSA approach versus more computationally intensive approaches such as full-Stokes models [*Morlighem et al.*, 2010] or hybrid models [*Pollard and DeConto*, 2009; *Hindmarsh*, 2004]. One way to approach this issue is to compute the magnitude of the vertical shear (in m/yr) between the bed and the surface of the PIG model, using a SSA model versus a full-Stokes model [*Morlighem et al.*, 2010]. The ratio of this shear to the depth-averaged velocity can be seen as a rate of departure from a plug-flow type ice flow (SSA) to the "real" ice flow as captured by a full-Stokes model. For the entire PIG, vertical shear remains lower than 1% of the overall depth-averaged velocity, except for fluxgates 10 and 11, where it reaches from 1% to 5% of the depth-averaged velocity. These results are similar for mass fluxes, which depend only on ice flow velocity (given that we assume a constant ice density and thickness). This implies that the SSA model is capable of efficiently capturing PIG's mass balance, within 1% accuracy over almost the entire mesh domain. Special attention must be however payed to gates 10 and 11, where the model choice between SSA and full-Stokes becomes more relevant. For the remainder of the study, we will therefore rely on the SSA approximation to model the mechanical response of PIG to variations in geothermal heat flux.

[11] For the SSA model, depth-averaged viscosity μ is non-linear, and follows a Norton-Hoff law [*Glen*, 1955]:

$$\mu = \frac{B}{2\dot{\varepsilon}_e^{\frac{n-1}{n}}} \tag{1}$$

where B is the depth-averaged ice hardness, n Glen's law exponent and $\dot{\varepsilon}_e$ the effective strain rate (defined as the second invariant of the strain rate tensor). B is temperature dependent and follows an Arrhenius law. A full thermal model is therefore needed to study the influence of geothermal heat flux on ice flow velocity. Here, we use the thermal model described in *Larour et al.* [2012b] and *Morlighem et al.* [2010], which includes conduction-advection in three directions. The model is run to steady state, which simplifies the energy equation to:

$$\rho c\, \mathbf{v} \cdot \nabla T = k_{th} \Delta T + \Phi \tag{2}$$

where T is the ice temperature, $\mathbf{v}$ the velocity vector, k_{th} the ice thermal conductivity, c the ice heat capacity, Φ the deformational heating, ρ the ice density, Δ the Laplace operator and ∇ the gradient operator. We refer the reader to *Larour et al.* [2012b] and *Morlighem et al.* [2010] for more details on the model implementation. Here, we are interested in the boundary condition at the ice/bed interface:

$$k_{th} \nabla T \cdot \mathbf{n} = G - \tau_b \cdot \mathbf{v_b} \tag{3}$$

where $\boldsymbol{\tau_b} \cdot \mathbf{v_b}$ is the heat generated by friction at the base, $\mathbf{v_b}$ is the basal velocity vector tangential to the glacier base plane, $\boldsymbol{\tau_b}$ the tangential component of the external force $\boldsymbol{\sigma} \cdot \mathbf{n}$, $\mathbf{n}$ the outward pointing normal vector, G the geothermal heat flux and $\mathbf{n}$ the normal vector to the ice/bed interface.

[12] Because temperature and velocity are coupled, both mechanical and thermal models must be iterated upon until convergence of the solution fields is satisfactory. As described in *Fastook* [1993], up to 30 iterations are needed. This makes a thermomechanical steady state solution computationally challenging.

[13] In addition, the mechanical model is heavily dependent on the basal drag coefficient, which is usually poorly known, and inferred using inverse methods and observed

surface velocities. This coefficient α relates basal stress $\boldsymbol{\tau_b}$ to the velocity $\mathbf{v_b}$ at the bed/ice interface:

$$\tau_b = -\alpha^2 \mathbf{v_b}. \quad (4)$$

[14] In order to determine α, we rely on inverse methods, which have been extensively documented in *MacAyeal* [1992, 1993], *Rommelaere and MacAyeal* [1997], *Larour et al.* [2005], *Vieli et al.* [2006], *Khazendar et al.* [2007, 2009], *Larour et al.* [2012b], and *Morlighem et al.* [2010]. A significant difference between our approach and the latter studies is that we invert α in steady state mode, similar to *Morlighem et al.* [2010]. This means that for each iteration of the inverse method, a thermal steady state is re-computed, using updated viscous and basal heating terms. This approach is necessary because variations in geothermal heat flux could have a strong influence on the distribution of heat through the ice sheet, which would then respond in a coupled thermomechanical way.

[15] Once the thermomechanical model is initialized (i.e., the basal drag coefficient is inverted for), we carry out two sampling analyses. In the first one, we sample the geothermal heat flux according to a statistical distribution, which reflects the internal variations and across differences between both data sets *Shapiro and Ritzwoller* [2004] and *Maule et al.* [2005]. For each sample, we re-compute the thermal regime of the ice sheet, along with the resulting depth-averaged ice hardness. We refer the reader to *Larour et al.* [2012b] and *Morlighem et al.* [2010] for more details on the method. Each geothermal heat flux sample is generated across the entire ice flow, assuming a normal statistical distribution. The choice of statistical distribution is of course critical in driving and assessing the propagation of uncertainties, and special care must be taken in using the distribution that best captures the uncertainty present in the geothermal heat flux. More details regarding this choice will be presented in Section 3 below.

[16] Each sample acquires values on a partition of the underlying mesh (shown in Figure 1). The partitioning algorithm is area-weighted, so that each partition of the mesh is of equal area. This avoids introducing area dependencies in the sampling analysis, where some partition might be more influential because of its disproportionate area. The mesh partition is created using the CHACO Software for Partitioning Graphs [*Hendrickson and Leland*, 1995]. The samples are generated by the DAKOTA framework [*Eldred et al.*, 2008] using a Latin-Hypercube engine, and output statistics such as average and standard deviation of ice hardness are also generated assuming best-fit to a normal distribution. For more details on the integration of DAKOTA, CHACO and ISSM, we refer the reader to *Larour et al.* [2012a]. In short, DAKOTA is a statistical engine that was tightly integrated within ISSM to facilitate data management and abstraction of statistical capabilities, with the goal of facilitating and making more robust ensemble type runs using ice flow models. By using this integrated framework, users can best concentrate on the design of experiments rather than the intricacies of statistical treatment of complex ice flow models.

[17] In the second analysis, we sample ice hardness B and compute mass fluxes across thirteen flux gates distributed uniformly across PIG (see Figure 1) using the 2D SSA mechanical model. To calibrate the sampling of B, we use the results of the previous sampling analysis, specifically the standard deviation s and mean of B. In this second analysis, the thermal regime remains steady state, and we rely exclusively on the 2D SSA equations to model the ice flow and corresponding mass fluxes. The goal of this analysis is to assess the forward propagation of errors in the ice hardness (resulting from errors in geothermal heat flux) through the steady state mechanical ice flow model. We are specifically interested in the impact on mass fluxes and the mass balance of PIG.

3. Data and Model Setup

[18] The model is setup using bedrock data from the 2004/05 AGASEA/BBAS survey [*Holt et al.*, 2006; *Vaughan et al.*, 2006] and completed using the 2009 Operation IceBridge campaign data [*Allen*, 2009]. Surface elevation comes from *Bamber et al.* [2009], surface temperatures from *Ettema et al.* [2009], and InSAR surface velocities used for inverting the basal drag coefficient come from *Rignot* [2008b].

[19] The geothermal heat flux G used to initialize our model needs to account for differences across both *Shapiro and Ritzwoller* [2004] and *Maule et al.* [2005] data sets, as well as internal variations due to errors and inconsistencies. Figure 2 shows Probability Density Functions (PDFs) for both data sets at the 1996 grounding line position. The *Shapiro and Ritzwoller* [2004] data set (in blue) follows a log-logistic distribution, with an average over West Antarctica of 107 mW/m^2. This distribution has very high tails, reflecting higher uncertainty at higher values of heat flux. The *Maule et al.* [2005] PDF follows a normal distribution, with a constant standard deviation of 9 mW/m^2 across the entire PIG. Given that computational capabilities in DAKOTA do not allow for sampling of a data set that results from the combination of several PDFs, we adopt a strategy of finding an equivalent normal distribution that captures both internal variations in and differences across both data sets. This new distribution, plotted in red in Figure 2, has a mean equal to the average of both data sets means, and a standard deviation calibrated so that the lower tail (where the cumulative density function is equal to 0.01) is equal to the average of the *Shapiro and Ritzwoller* [2004] and *Maule et al.* [2005] data set tails. This new distribution is therefore centered on the average of both data sets, and has errors associated that fall between both data set error ranges. Unfortunately, the higher tails of *Shapiro and Ritzwoller* [2004] cannot be captured by a normal (or uniform) distribution, but our choice of mean and standard deviation ensures that we at least offset mean and standard deviation toward higher values as captured by the *Shapiro and Ritzwoller* [2004] data set. In addition, we also associate to the new normal distribution a uniform distribution, centered on the same average, but ranging between -3s and 3s (where s is the standard deviation). This uniform distribution will also be used in sampling studies, along with the normal distribution, to test for the influence of the geothermal heat flux PDD shape in model runs.

[20] The *Shapiro and Ritzwoller* [2004] and *Maule et al.* [2005] data sets are taken from the SeaRISE project (http://websrv.cs.umt.edu/isis/index.php/SeaRISE_Assessment, 2011), which is regridded (using linear interpolation) from $2^\circ \times 2^\circ$

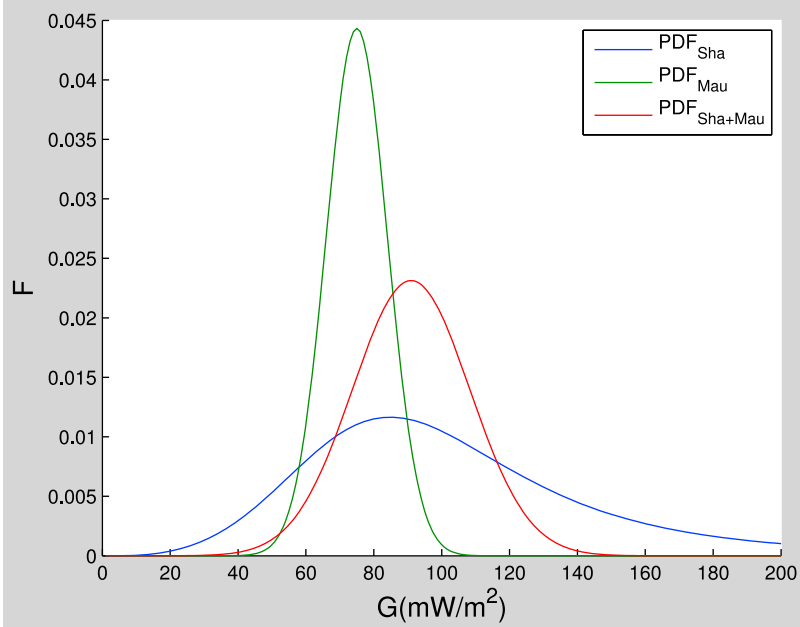

Figure 2. Probability density functions (PDFs) of geothermal heat flux for the *Shapiro and Ritzwoller* [2004] and *Maule et al.* [2005] data sets (in blue and green respectively). The *Maule et al.* [2005] data set carries a constant error of 27 mW/m^2, which translates into a standard deviation s of 9 mW/m^2 assuming a Gaussian distribution of the error (3s = 27 mW/m^2 for 99% of the distribution). The *Shapiro and Ritzwoller* [2004] data set assumes a Log-logistic distribution of the error, which carries more elongated upper tails. We refer the reader to *Shapiro and Ritzwoller* [2004] for more details on this distribution. A PDF resulting from a combination of both data sets is displayed in red. This PDF describes a Gaussian distribution, with the lower tail calibrated to fall between both tails of the *Maule et al.* [2005] Gaussian distribution and the *Shapiro and Ritzwoller* [2004] log-logistic distribution. All PDFs are normalized to 1, and are taken at the 1996 grounding line position, taken from *Rignot* [2008a].

(600 to 1,000 km) for the *Shapiro and Ritzwoller* [2004] data set and 5 km for the *Maule et al.* [2005] data set; to the 5 km resolution SeaRISE grid. Both data sets are then interpolated from the SeaRISE grid onto the anisotropic mesh (average resolution 5 km) using bilinear interpolation. Using SeaRISE data sets ensures that the results of this study can be replicated easily.

[21] The model mesh comprises 15,000 horizontal elements, extruded vertically over 10 layers. Horizontal resolution is approximately 5 km everywhere, and vertical resolution ranges from 300 m at the thickest places to 1 m at the thinnest places. The number of degrees of freedom solved for is 150,000, which requires full-use of the parallel technologies implemented in ISSM. Indeed, using the NASA Advanced Supercomputing (NAS) Pleiades cluster, on 80 CPUS, each sample run takes approximately 8 s. The number of samples used in both studies (sampling of geothermal heat flux and sampling of depth-averaged ice hardness) is 2,000 (see Figure 1), which takes approximately 4 hours. This number is inspired from *Larour et al.* [2012a], where it was shown that statistical results were strongly convergent when relying on 10 to 25 samples per partition. The *Larour et al.* [2012a] analysis was however based on the Monte-Carlo method. Here, we rely on the Latin-Hypercube method, which is more efficient at sampling, and captures distribution tails better due to its "binned" approach to sampling. We therefore feel confident that our number of samples is statistically significant for the type of analysis considered here.

4. Results

[22] Results for the model initialization and model setup are presented in Figure 3. As previously remarked, the *Maule et al.* [2005] and *Shapiro and Ritzwoller* [2004] data sets differ by 20 to 80 mW/m^2, with the largest differences near the boundary between PIG and Thwaites Glacier. On the upper part of PIG's tributaries, both data sets are similar, with a general trend of increasing differences from North to South. The modeled depth-averaged ice hardness B (in kPa yr$^{-1/3}$) is shown in Figure 3d. Ice hardness is computed using the converged steady state thermomechanical ice flow model of PIG, based on the new combined geothermal heat flux (see Section 3) and on model inversion of the basal drag coefficient (Figure 3e). B follows the tributaries, with lower values in the faster-flowing parts of PIG, where frictional and viscous heating are most important, resulting in softer ice, and higher-values inland and toward the ice divide, where temperatures are colder, and friction at the base negligible, resulting in harder ice. The basal drag coefficient α (in (Pa.s/m)$^{1/2}$) follows similar trends, with very low values in fast-flowing tributaries, and in the main trunk of the glacier. Such values are indeed necessary to capture the low-resistance of the ice/bed interface to high driving stresses, and large resulting ice flow velocities

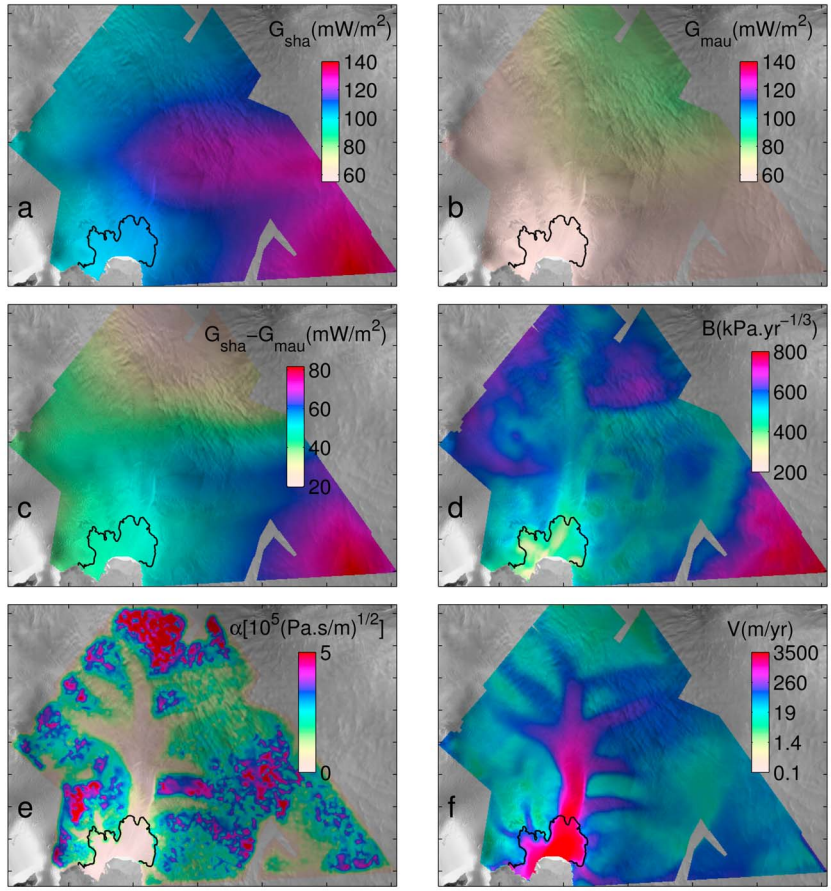

Figure 3. Model inputs and results for Pine Island Glacier, West Antarctica: (a) geothermal heat flux from *Shapiro and Ritzwoller* [2004] (2° × 2° resolution, downscaled to 5 km resolution using linear interpolation), (b) geothermal heat flux from *Maule et al.* [2005] (5 km resolution data set reinterpolated onto the mesh using linear interpolation), (c) difference between *Shapiro and Ritzwoller* [2004] and *Maule et al.* [2005] geothermal heat fluxes, (d) modeled depth-averaged ice hardness B in kPa yr$^{-1/3}$, (e) basal drag coefficient α in (Pa s/m)$^{1/2}$ inverted using InSAR surface velocities from *Rignot* [2008a], and (f) modeled velocity magnitude in (m/yr). The 1996 grounding line position from *Rignot* [2008a] is plotted in black.

(Figure 3f). The average difference between modeled velocity and surface velocity is approximately 20 m/yr, and we refer the reader to *Morlighem et al.* [2010] for a more detailed analysis of the basal drag coefficient patterns, as well as implications for the dynamics of PIG.

[23] Results for the sampling analysis of geothermal heat flux are presented in Figures 4 and 5. In Figure 4, we show the heat flux $\boldsymbol{\tau_b} \cdot \mathbf{v_b}$ in mW/m^2 generated by basal friction (Figure 4a), the heat flux $HTr(\sigma\dot{\varepsilon})$ in W/m^2 generated by viscous deformation (Figure 4b), for reference, the uncertainty in the ice thickness data set used to initialize the model (from the 2009 Operation IceBridge campaign, courtesy of CReSIS) based on cross-over analysis (Figure 4c), and the uncertainty $\Delta B/B$ (in %) in depth-averaged ice hardness (ΔB is equal to twice the three standard deviations of the ice-hardness output statistical distribution) (Figure 4d). In Figure 5, we show histogram and corresponding scatterplots for locations 1 and 2 respectively (as marked in Figure 4d). These results show that $\Delta B/B$ remains small across the entire ice stream, ranging from 0.1% in mountainous areas to 15% in the middle of the main glacier and most of its upstream tributaries. These values are comparable to the magnitude of the uncertainties found in the thickness data set (Figure 4c) used to initialize the model, except for certain locations near shear margins and subglacial mountain ranges where such uncertainty can reach up to 30%. We also see that $\Delta B/B$ is structured in channels that follow the main tributaries, and matches the distribution pattern of B (Figure 3c). Both histograms show Gaussian type distributions, irrespective of their location across PIG. The corresponding scatterplots exhibit a downward trend, which is expected, as ice hardness should soften the warmer the ice, which should occur more often for higher values of geothermal heat flux. Local variations over short distances (5 km) are abrupt, with drops in $\Delta B/B$ of almost 4 orders of magnitude between tributaries and mountainous areas. Heat fluxes resulting from basal friction and viscous deformation are orders of magnitude higher than the geothermal heat flux across the main glacier and its northern tributaries. In the interior of the ice sheet, where ice velocity is small, geothermal heat flux and both viscous and basal heating are on the same order of magnitude, which should increase the sensitivity of ice hardness to geothermal flux errors.

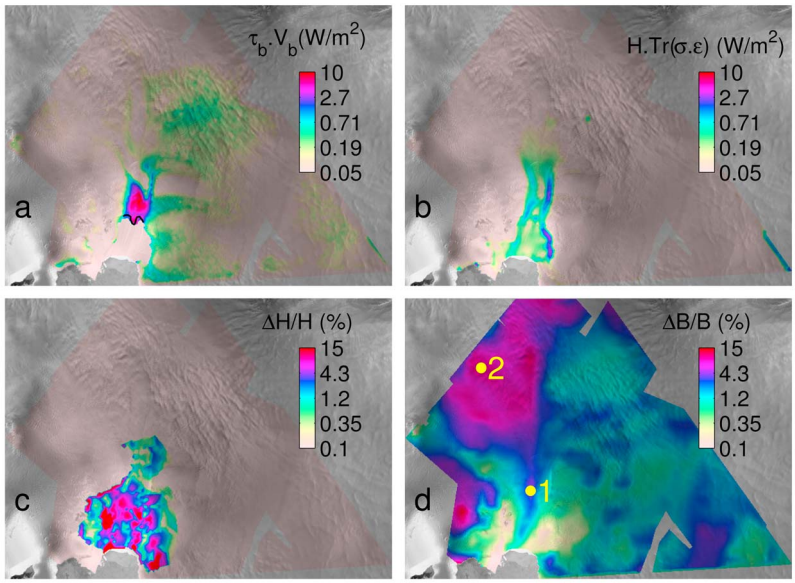

Figure 4. (a) Heat flux $\boldsymbol{\tau_b} \cdot \mathbf{v_b}$ (where $\boldsymbol{\tau_b}$ and $\mathbf{v_b}$ are respectively the friction force and velocity at the ice/bed interface) in mW/m^2 from basal friction, (b) heat flux $HTr(\sigma\dot{\varepsilon})$ (where H is the ice thickness, σ and $\dot{\varepsilon}$ the stress and strain rate tensors respectively and Tr the trace operator) in mW/m^2 from viscous deformation near the ice/bed interface, (c) thickness uncertainty $\Delta H/H$ (in %, logarithmic scale) for the 2009 Operation IceBridge data set, courtesy of CReSIS, computed from cross-over analysis, and (d) ice hardness uncertainty $\Delta B/B$ (in %, logarithmic scale) modeled from a sampling study, where geothermal heat flux is sampled using a uniform statistical distribution between the *Maule et al.* [2005] and *Shapiro and Ritzwoller* [2004] data sets. For locations 1,2 (marked in yellow) corresponding ice hardness histograms are displayed in Figures 5a and 5b, as well as scatterplots (Figures 5c and 5d).

[24] Figure 6 and Table 1 present the results of the second analysis, in which we sample ice hardness according to the mean and standard deviation obtained from the first sampling analysis. We compute corresponding output statistics for the mass fluxes at thirteen fluxgates laid out across PIG (Figure 1). Figure 6 shows in green the statistical distributions for each fluxgate. For comparison, we display in red histograms from *Larour et al.* [2012a], in which ice thickness is sampled according to cross-over errors from CReSIS. Table 1 summarizes statistics for both sets of results, specifically the mass flux average (in Gt/yr) and corresponding uncertainties (in %) for all thirteen fluxgates. These results demonstrate the existence of two areas: 1) the downstream area of PIG, near fluxgates 1–4, and fluxgates 10–13, where mass flux uncertainty generated by errors in ice thickness are orders of magnitude larger than uncertainties generated by errors in geothermal heat flux; 2) the upstream area of PIG, near fluxgates 5–9, which defines the onset of the trunk of the glacier, where mass flux uncertainties generated by errors in geothermal heat flux and ice thickness are on the same order of magnitude. Both areas are well defined, and correspond to very different types of ice flow deformation and thermal regime. The upper part of the glacier is where uncertainties in ice hardness are most important (near location 2), and where internal viscous heating as well as heating resulting from basal friction is lowest (Figure 4b). It also corresponds to an area where geothermal heat flux is high, and on the same order of magnitude as heating from internal deformation and basal friction. On the other hand, the lower part of the ice stream is where errors in ice thickness are most important, and where viscous heating and heating resulting from basal friction are orders of magnitude higher than geothermal heat flux. This area will therefore be weakly sensitive to errors in geothermal heat flux, and will be mainly sensitive to errors in the specification of the ice sheet/ice shelf geometry (thickness, bedrock and surface position).

5. Discussion

[25] The relative variation $\Delta B/B$ (Figure 4d) over PIG appears highly dissymmetrical, with a clear cut between the southern and northern parts of the glacier, delineated by the central trunk of the ice stream. Figures 4a and 4b provide an explanation for this effect, showing that heat originating from basal friction dominates on the southern part of the basin, which tends to dampen any variations in B due to errors in geothermal heat flux. On the northern part of the glacier however, heat originating from basal friction and viscous deformation is on the same order of magnitude as heat available from geothermal energy. The consequence is therefore a higher sensitivity to errors in the specification of geothermal heat flux. An analysis of the distribution histograms for B at two different locations (1 and 2 in Figure 4d) shows very similar distributions, Gaussian in nature. This demonstrates a very linear behavior of the SSA ice flow model with respect to errors in model inputs given the nonlinear nature of the material law used in the model. We refer the reader to *Larour et al.* [2012a] for more details on this aspect of the SSA model.

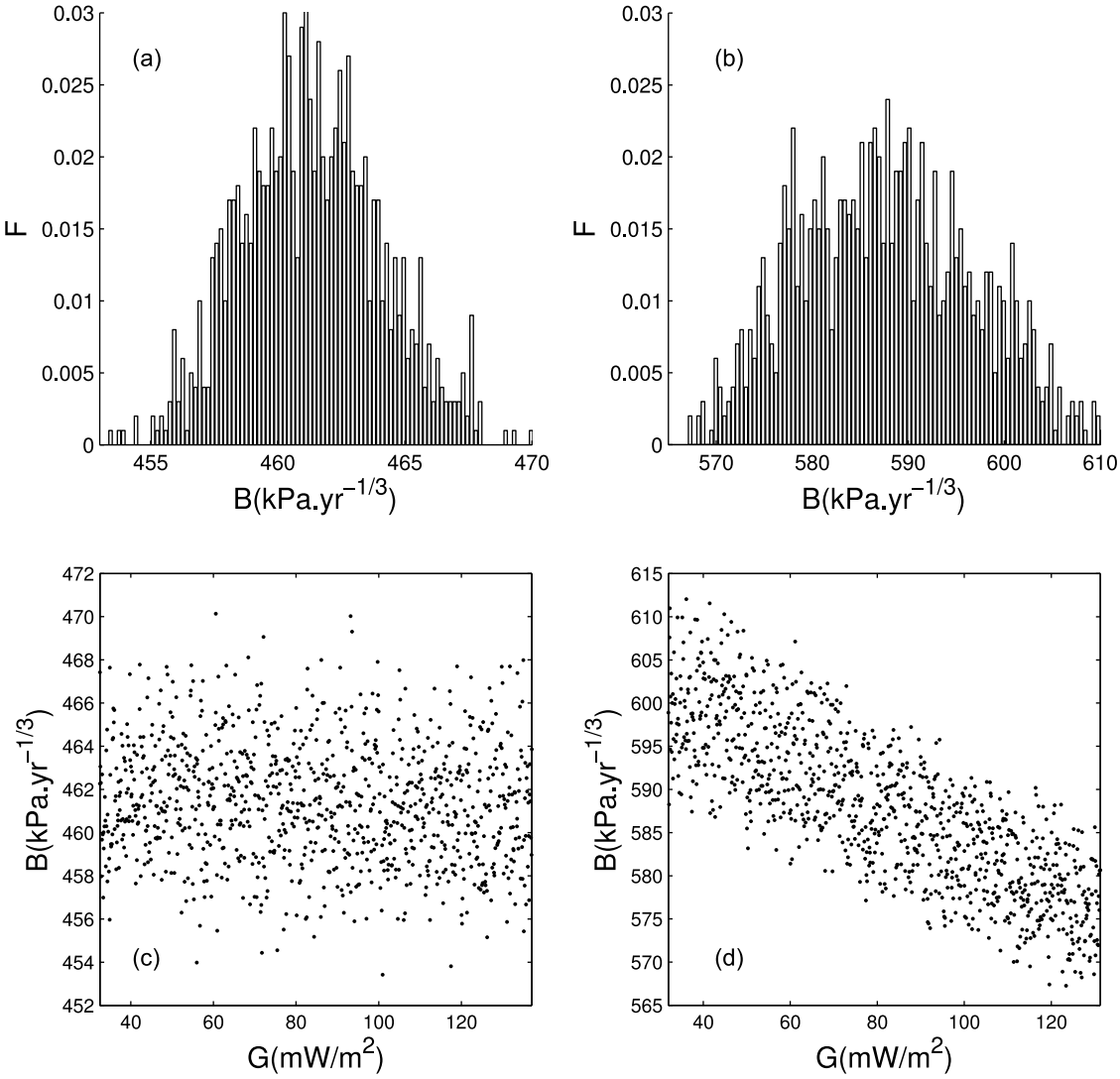

Figure 5. (a, b) Ice hardness histograms for locations 1 and 2 respectively (marked yellow on Figure 4d). The statistical bin size for each histogram is 10 samples. x-axis is depth-averaged ice hardness in kPa yr$^{-1/3}$, y-axis is the output frequency. (c, d) Scatterplots for locations 1 and 2 respectively. x-axis is the local geothermal heat flux G (in mW/m^2) as sampled using DAKOTA. y-axis is the local ice hardness response to the sampled geothermal heat flux, using the ISSM thermomechanical steady state model.

[26] $\Delta B/B$ exhibits significant variations compared to ice thickness (see Figure 4c) only in the upper part of the tributary, where relative errors in ice hardness can reach up to 15%. The absence of reliable error estimates for the AGASEA/BBAS survey in this area constrains our interpretation of the results. In the lower part of the glacier however, extensive cross-over error data are available from the CReSIS data set, which shows that $\Delta H/H$ can reach up to 30%, while $\Delta B/B$ remains below 1%. We attribute this to the predominance of basal friction in the heat balance of the ice sheet (see Figure 4a), which precludes any significant variations in B from developing. It is also due to the proximity of the ice shelf where errors in ice thickness are significant, due to the transition from grounded to ungrounded ice, which is difficult to capture in Ground Penetrating Radar surveys of the area [*Allen*, 2009]. In addition, geothermal heat flux is nil on the ice shelf, which translates into a zero constraint on geothermal heat flux variations and should therefore dampen the sensitivity of ice hardness to geothermal heat flux. However, the extent to which such lack of variations propagate upstream is probably limited, given the advective nature of the thermal regime near the grounding line, where basal sliding is intense, and fast ice-flow well developed.

[27] In terms of mass fluxes, Figure 6 and Table 1 show that errors in the specification of ice hardness (computed in our first sampling analysis) impact mass flux at the 13 fluxgates across PIG much less than errors in the specification of ice thickness. Once again, statistical histograms for mass fluxes appear Gaussian in nature, which confirms the linear behavior of the SSA model that we commented on in the previous section. Errors in mass fluxes due to uncertainties in ice hardness B are small, below 1% in general, indicating a weak influence of the geothermal heat flux errors on the resulting mass balance of the glacier. On the opposite, errors in mass flux due to uncertainties in ice

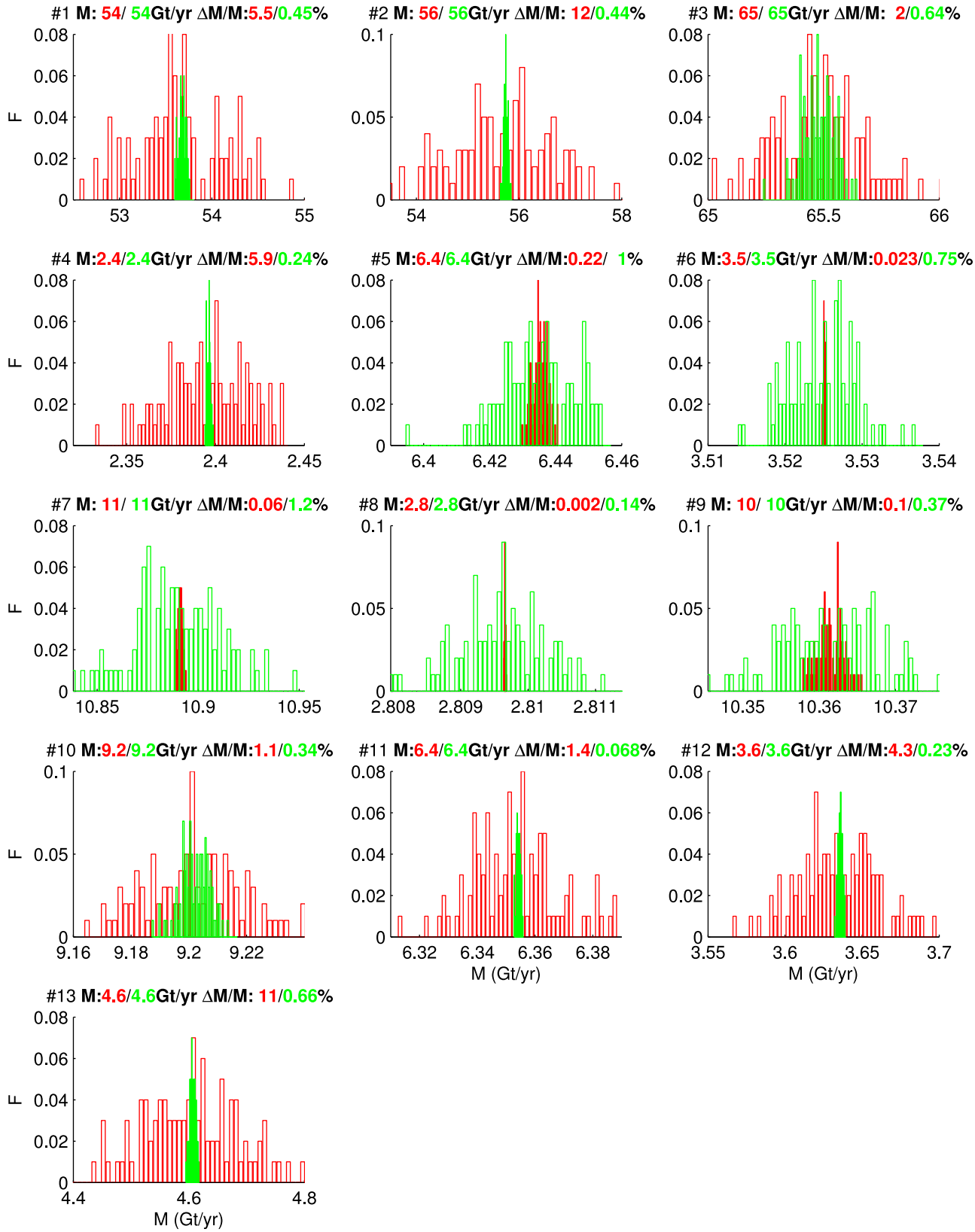
#1 M: 54/ 54Gt/yr ΔM/M:5.5/0.45%
#2 M: 56/ 56Gt/yr ΔM/M: 12/0.44%
#3 M: 65/ 65Gt/yr ΔM/M: 2/0.64%
#4 M:2.4/2.4Gt/yr ΔM/M:5.9/0.24%
#5 M:6.4/6.4Gt/yr ΔM/M:0.22/ 1%
#6 M:3.5/3.5Gt/yr ΔM/M:0.023/0.75%
#7 M: 11/ 11Gt/yr ΔM/M:0.06/1.2%
#8 M:2.8/2.8Gt/yr ΔM/M:0.002/0.14%
#9 M: 10/ 10Gt/yr ΔM/M:0.1/0.37%
#10 M:9.2/9.2Gt/yr ΔM/M:1.1/0.34%
#11 M:6.4/6.4Gt/yr ΔM/M:1.4/0.068%
#12 M:3.6/3.6Gt/yr ΔM/M:4.3/0.23%
#13 M:4.6/4.6Gt/yr ΔM/M: 11/0.66%
F
M (Gt/yr)

Figure 6

Table 1. Mass Flux Sampling Analysis Results for the Thirteen Fluxgates Specified in Figure 3d[a]

Profile	M_G (Gt/yr)	M_H (Gt/yr)	$\Delta M_G/M_G$ (%)	$\Delta M_H/M_H$ (%)
1	53.69	53.7	0.45	5.5
2	55.75	55.76	0.44	12
3	65.48	65.48	0.64	2
4	2.396	2.396	0.24	5.9
5	6.436	6.435	1	0.22
6	3.525	3.525	0.75	0.023
7	10.89	10.89	1.2	0.06
8	2.81	2.81	0.14	0.002
9	10.36	10.36	0.37	0.1
10	9.203	9.203	0.34	1.1
11	6.354	6.354	0.068	1.4
12	3.636	3.636	0.23	4.3
13	4.607	4.607	0.66	11

[a]For each fluxgate (1–13), we provide two sets of results. The first set (M_B and $\Delta M_B/M_B$) corresponds to the mean (in Gt/yr) and relative variation (in %) for the mass flux sampling analysis where the sampled input parameter is ice hardness B (see Figure 6, in green). The second set (M_H and $\Delta M_H/M_H$) corresponds to the mean and relative variation for the mass flux sampling analysis where the sampled input parameter is ice thickness (see Figure 6, in red). For both studies, relative mass flux variation are computed using the statistical mean of the mass flux, and an absolute variation ΔM equal to double the three standard deviations 3 s of the mass flux distribution.

thickness H are consistently higher than 1% on the lower part of the ice stream, and range from 0.002% to 0.22% on the upper part of the ice stream. As was discussed previously, reliable error estimates for the AGASEA/BBAS survey are not available, which makes any interpretation difficult. To remedy this issue, we increased the uncertainty on ice thickness in the upper part of PIG (where CReSIS data becomes unavailable) to a constant 10 m everywhere, which we used to calibrate a new statistical distribution for ice thickness. The results of the new sampling analysis yielded uncertainties in mass fluxes reaching 1% in the upper gates (5–9). From these results, we conclude that ice thickness is the most critical factor for constraining the mass balance of PIG, with geothermal heat flux playing a significant role only in the interior of the basin.

[28] Our conclusions cannot of course be extended to transient ice flow models, because our analysis is based on a thermomechanical steady state regime. However, it is almost certain that when carried forward in time, such uncertainties will increase significantly. Further studies on transient ice flow models are therefore strongly warranted. Factors that could increase uncertainty include among others strong dynamic effects that occur at the grounding line, where studies have consistently demonstrated a strong link between mass flux and ice thickness [*Schoof*, 2007a, 2007b; *Nowicki and Wingham*, 2008; *Durand et al.*, 2009], evolution of the basal friction and resulting heat at the ice/bed interface, evolution of the accumulation rate in the interior of the ice sheet, where vertical advection dominates the thermal regime, etc. Our thermomechanical steady state model provides an assessment of the uncertainty propagated in a thermally stable ice flow. The largest uncertainty for PIG will however originate mainly from transients in the evolution of the melting under the ice shelf. Such melting rates have been shown to vary significantly over several decades [*Schodlok et al.*, 2012], and it is believed that they are responsible for the acceleration of PIG in the past twenty years [*Rignot*, 2008b]. In our model, such melting rates are not captured, and even less so the uncertainty that they propagate into ice flow models. This is because melting rates are accounted for in transient ice flow models through the mass transport equations. Such equations are used to compute the thinning rate of a glacier using the depth-averaged velocity divergence, the surface mass balance and the melting rate at the water/bed interface. In addition, strong melting rates under the ice shelf lead to the formation of cavities under the ice shelf, as shown by recent gravity results from Operation IceBridge [*Studinger et al.*, 2012] and from *Jenkins et al.* [2010]. With melting rates as high as 35 m/yr [*Schodlok et al.*, 2012], such cavities will enlarge as grounding lines retreat, which in turn will lead to strong variations in melting rates. Such feedback mechanisms will strongly influence the evolution of PIG, in a way that is currently not represented in our study.

[29] Another aspect of the study that should be investigated further and that is not captured by our methodology is the influence of the combination of uncertainties in several inputs at the same time. Our sampling analysis is carried out one-at-a-time for ice thickness, then for ice hardness. However, non-linear effects could probably develop in which specific values of both inputs would yield increased variations in the mass outflux at certain gates. This could for example occur were a geothermal heat flux maximum to coincide with an increase in the driving stress (from thickness variations) near a fluxgate. This non-linear effect is hard to capture without some type of dynamic adaptation in the sampling algorithm.

[30] In a similar way, our results are only valid for fast flowing ice streams such as PIG, where internal vertical shearing remains negligible. We therefore expect our conclusions to hold true for most ice streams in Antarctica, such as ice streams flowing into the Ross and Ronne ice shelves. This should however be tempered by the fact that our model setup involves inversion of the basal drag coefficient. This is a powerful method to initialize ice flow models, but it also tends to lump into one parameter, the basal drag coefficient, a lot of missing processes not represented in our model, as

Figure 6. Histograms for mass flux sampling studies across gates specified in Figure 1. Results in red correspond to sampling of the ice thickness, while results in green correspond to sampling of the depth-averaged ice hardness. For both studies, we assume parameters can be sampled using a normal statistical distribution. For ice thickness, the three standard deviations 3 s is taken equal to half the cross-over errors of the 2009 Operation IceBridge thicknesses (courtesy of CReSIS). For ice hardness, results of a previous sampling analysis (see Figures 4d and 5) are used to specify the mean and standard deviation. Histograms are based on a bin size of 10. In addition to the histograms, we provide sampling analysis results such as the mass flux statistical average (in Gt/yr), and the mass flux relative variation $\Delta M/M$ (in %), where ΔM is equal to twice the three standard deviations 3 s of the distribution and M is the average of the mass flux. For each fluxgate, the x-axis of the histogram corresponds to mass flux (in Gt/yr), and the y-axis is the frequency of the mass flux sample computed by our forward ice flow model.

well as data set errors such as incompatibilities between InSAR surface velocities and thickness data [*Morlighem et al.*, 2011; *Seroussi et al.*, 2011]. This probably ends up making the model overly sensitive to basal drag, and heat resulting from friction at the ice/bed interface. Another issue is also the fact that quantifying errors in the basal drag coefficient is difficult, as it is not an observable quantity, but the result of an inversion model itself based on the adjoint of the forward mechanical ice flow model [*Larour et al.*, 2012b]. In order to correctly assess how much is lumped in the basal drag coefficient, one would need to carry out an extensive study of the uncertainty in basal friction generated by the inversion model. This type of analysis would be computationally expensive, as it would involve sampling of the inversion model itself, using errors in model inputs such as InSAR surface velocities. This lies outside the scope of the present study, but it warrants further analysis. Similarly, if the uncertainty in basal friction was quantified, the present study and *Larour et al.* [2012a] could be the basis for an exhaustive evaluation of how errors in basal friction, geothermal heat flux and ice thickness propagate forward using a steady state thermomechanical ice flow model.

[31] For ice flow regimes where internal vertical shearing dominates, such as in the interior of the ice sheet where the ice/bed interface is frozen, geothermal heat flux will certainly play a more significant role. As an example, Figure 4d shows that in the interior of the ice sheet, at the boundary between PIG and Thwaites Glacier, $\Delta B/B$ can reach values of up to 5%. This corresponds to an area where heat from internal deformation, basal friction and geothermal energy are all on the same order of magnitude. It also corresponds to a place of high basal friction (see Figure 3d) and cold rigid ice. Although the model needs to be considered carefully in these areas given the nature of the flow regime for an SSA formulation, these results seem to corroborate the fact that increased uncertainty in the mass balance of the ice sheet will result from errors in the specification of geothermal heat flux the more inland the area of interest lies. In addition, as seen in Figures 3a and 3b, geothermal heat flux tends to increase deep into the interior of the WAIS. As suggested by the log-logistic distribution from *Shapiro and Ritzwoller* [2004], uncertainties in geothermal heat flux will increase inland, which compounds the need for further studies. This result provides a compelling argument for the need to carry out further extensive sampling analyses using higher-order thermomechanical models in the interior of the WAIS, where geothermal heat fluxes are important and poorly constrained.

6. Conclusions

[32] For fast flowing ice streams such as PIG, our results reveal that ice hardness is influenced by geothermal energy in the slow moving areas of the glacier preferentially. For the fast moving areas, this influence is reduced. In addition, we quantify the uncertainty generated in mass fluxes across the entire ice stream from the forward propagation of the ice hardness errors using a steady state mechanical ice flow model. We demonstrate that the uncertainty resulting from ice hardness errors is smaller than the uncertainty resulting from errors in the ice thickness. We are also able to correlate ice hardness uncertainties to available heat at the ice/bedrock interface from viscous heating and basal friction. However, this correlation breaks down in the interior of the ice sheet, where higher order models are probably needed. Our sampling analyses also indicate that at any given time, mass flux uncertainties due to geothermal heat flux errors remain below 1%, which is smaller than the equivalent uncertainties due to ice thickness errors. This has strong implications for the modeling community, as our study tends to indicate that models of mass balance in Antarctica, especially in fast flowing ice streams, stand to gain the most from improved constraints on ice thickness. In the interior of the ice sheet, where geothermal energy is one of the most critical thermal drivers, such conclusions cannot be extended, and further sampling analyses are needed to assess which parameter is most critical in controlling ice flow.

[33] **Acknowledgments.** This work was performed at the Jet Propulsion Laboratory, California Institute of Technology, and the Department of Earth System Science, University of California Irvine, under a contract with the National Aeronautics and Space Administration, Cryospheric Sciences Program and MAP Program. The authors would like to acknowledge Operation IceBridge data used in the study, as well as CReSIS data generated from NSF grant ANT-0424589 and NASA grant NNX10AT68G. Hélène Seroussi was supported by an appointment to the NASA Postdoctoral Program at the Jet Propulsion Laboratory, California Institute of Technology, administered by Oak Ridge Associated Universities through a contract with NASA. We would also like to acknowledge R. Gladstone, the Associate Editor Poul Christoffersen and the other anonymous reviewers for their review and insights into the manuscript.

References

Allen, C. (2009), IceBridge MCoRDS L2 Ice Thickness, http://nsidc.org/data/irmcr2.html, Natl. Snow and Ice Data Cent., Boulder, Colo. [Updated 2012].

Bamber, J. L., J. L. Gomez-Dans, and J. A. Griggs (2009), A new 1 km digital elevation model of the Antarctic derived from combined satellite radar and laser data—Part 1: Data and methods, *Cryosphere*, *3*, 101–111.

Blatter, H. (1995), Velocity and stress-fields in grounded glaciers: A simple algorithm for including deviatoric stress gradients, *J. Glaciol.*, *41*, 333–344.

Durand, G., O. Gagliardini, B. de Fleurian, T. Zwinger, and E. Le Meur (2009), Marine ice sheet dynamics: Hysteresis and neutral equilibrium, *J. Geophys. Res.*, *114*, F03009, doi:10.1029/2008JF001170.

Eldred, M. S., et al. (2008), DAKOTA, a multilevel parallel object-oriented framework for design optimization, parameter estimation, uncertainty quantification, and sensitivity analysis, Version 4.2 User's Manual, *Tech. Rep. SAND2006-6337*, Sandia Natl. Lab., Albuquerque, N. M.

Ettema, J., M. R. van den Broeke, E. van Meijgaard, W. J. van de Berg, J. L. Bamber, J. E. Box, and R. C. Bales (2009), Higher surface mass balance of the Greenland Ice Sheet revealed by high-resolution climate modeling, *Geophys. Res. Lett.*, *36*, L12501, doi:10.1029/2009GL038110.

Fastook, J. (1993), The finite-element method for solving conservation equations in glaciology, *Comput. Sci. Eng.*, *1*(1), 55–56.

Giering, R., and T. Kaminski (1998), Recipes for adjoint code construction, *ACM Trans. Math. Software*, *24*, 437–474.

Glen, J. (1955), The creep of polycrystalline ice, *Proc. R. Soc. A*, *228*, 519–538.

Greve, R. (1997a), A continuum-mechanical formulation for shallow polythermal ice sheets, *Philos. Trans R. Soc. A*, *355*, 921–974.

Greve, R. (1997b), Application of a polythermal three-dimensional ice sheet model to the Greenland Ice Sheet: Response to steady-state and transient climate scenarios, *J. Clim.*, *10*, 901–918.

Hansen, I., and R. Greve (1996), Polythermal modelling of steady states of the Antarctic ice sheet in comparison with the real world, *Ann. Glaciol.*, *23*, 382–387.

Hascoët, L. (2004), Tapenade: A tool for automatic differentiation of programs, in *Proceedings of 4th European Congress on Computational Methods, ECCOMAS'2004*, pp. 1–14, Univ. of Jyväskylä, Jyväskylä, Finland.

Heimbach, P., and V. Bugnion (2009), Greenland ice-sheet volume sensitivity to basal, surface and initial conditions derived from an adjoint model, *Ann. Glaciol.*, *50*, 67–80.

Hendrickson, B., and R. Leland (1995), The Chaco user's guide, version 2.0, *Tech. Rep. SAND-95-2344*, Sandia Natl. Lab., Albuquerque, N. M.

Hindmarsh, R. (2004), A numerical comparison of approximations to the Stokes equations used in ice sheet and glacier modeling, *J. Geophys. Res.*, *109*, F01012, doi:10.1029/2003JF000065.

Holt, J., D. Blankenship, D. Morse, D. Young, M. Peters, S. Kempf, T. Richter, D. Vaughan, and H. Corr (2006), New boundary conditions for the West Antarctic Ice Sheet: Subglacial topography of the Thwaites and Smith glacier catchments, *Geophys. Res. Lett.*, *33*, L09501, doi:10.1029/2005GL025588.

Jenkins, A., P. Dutrieux, S. Jacobs, S. McPhail, J. Perrett, A. Webb, and D. White (2010), Observations beneath pine island glacier in west Antarctica and implications for its retreat, *Nat. Geosci.*, *3*, 468–472.

Johnson, J. (2002), A basal water model for ice sheets, PhD thesis, Univ. of Maine, Orono.

Kerr, A., and P. Huybrechts (1999), The response of the East Antarctic ice-sheet to the evolving tectonic configuration of the Transantarctic Mountains, *Global Planet. Change*, *23*, 213–229.

Joughin, I., B. Smith, I. Howat, T. Scambos, and T. Moon (2010), Greenland flow variability from ice-sheet-wide velocity mapping, *J. Glaciol.*, *56*, 416–430.

Khazendar, A., E. Rignot, and E. Larour (2007), Larsen B Ice Shelf rheology preceding its disintegration inferred by a control method, *Geophys. Res. Lett.*, *34*, L19503, doi:10.1029/2007GL030980.

Khazendar, A., E. Rignot, and E. Larour (2009), Roles of marine ice, rheology, and fracture in the flow and stability of the Brunt/Stancomb-Wills Ice Shelf, *J. Geophys. Res.*, *114*, F04007, doi:10.1029/2008JF001124.

Larour, E., E. Rignot, I. Joughin, and D. Aubry (2005), Rheology of the Ronne Ice Shelf, Antarctica, inferred from satellite radar interferometry data using an inverse control method, *Geophys. Res. Lett.*, *32*, L05503, doi:10.1029/2004GL021693.

Larour, E., J. Schiermeier, E. Rignot, H. Seroussi, M. Morlighem, and J. Paden (2012a), Sensitivity analysis of Pine Island Glacier ice flow using ISSM and DAKOTA, *J. Geophys. Res.*, *117*, F02009, doi:10.1029/2011JF002146.

Larour, E., H. Seroussi, M. Morlighem, and E. Rignot (2012b), Continental scale, high order, high spatial resolution, ice sheet modeling using the Ice Sheet System Model (ISSM), *J. Geophys. Res.*, *117*, F01022, doi:10.1029/2011JF002140.

Le Brocq, A., A. Payne, M. Siegert, and R. Alley (2009), A subglacial water-flow model for west Antarctica, *J. Glaciol.*, *55*(193), 879–888.

MacAyeal, D. (1989), Large-scale ice flow over a viscous basal sediment: Theory and application to Ice Stream B, Antarctica, *J. Geophys. Res.*, *94*, 4071–4087.

MacAyeal, D. (1992), The basal stress distribution of Ice Stream E, Antarctica, Inferred by Control Methods, *J. Geophys. Res.*, *97*, 595–603.

MacAyeal, D. (1993), Binge/purge oscillations of the Laurentide ice-sheet as a cause of the North-Atlantics Heinrich events, *Paleoceanography*, *8*, 775–784.

Maule, C. F., M. E. Purucker, N. Olsen, and K. Mosegaard (2005), Heat flux anomalies in Antarctica revealed by satellite magnetic data, *Science*, *309*, 464–467.

Morlighem, M., E. Rignot, H. Seroussi, E. Larour, H. Ben Dhia, and D. Aubry (2010), Spatial patterns of basal drag inferred using control methods from a full-Stokes and simpler models for Pine Island Glacier, West Antarctica, *Geophys. Res. Lett.*, *37*, L14502, doi:10.1029/2010GL043853.

Morlighem, M., E. Rignot, H. Seroussi, E. Larour, H. Ben Dhia, and D. Aubry (2011), A mass conservation approach for mapping glacier ice thickness, *Geophys. Res. Lett.*, *38*, L19503, doi:10.1029/2011GL048659.

Nowicki, S. M. J., and D. J. Wingham (2008), Conditions for a steady ice sheet-ice shelf junction, *Earth Planet. Sci. Lett.*, *265*, 246–255.

Pattyn, F. (1996), Numerical modelling of a fast-flowing outlet glacier: Experiments with different basal conditions, *Ann. Glaciol.*, *23*, 237–246.

Pattyn, F. (2003), A new three-dimensional higher-order thermomechanical ice sheet model: Basic sensitivity, ice stream development, and ice flow across subglacial lakes, *J. Geophys. Res.*, *108*(B8), 2382, doi:10.1029/2002JB002329.

Pollard, D., and R. DeConto (2009), Modelling West Antarctica ice sheet growth and collapse through the past five million years, *Nature*, *458*, 329–332.

Pollard, D., R. M. DeConto, and A. A. Nyblade (2005), Sensitivity of Cenozoic Antarctic ice sheet variations to geothermal heat flux, *Global Planet. Change*, *49*, 63–74.

Rignot, E. (2008a), PALSAR studies of ice sheet motion in Antarctica, paper presented at 2nd Joint PI Symposium of ALOS Data Nodes for ALOS Science Program, Eur. Space Agency, Rhodes, Greece, 3–7 Nov.

Rignot, E. (2008b), Changes in West Antarctic ice stream dynamics observed with ALOS PALSAR data, *Geophys. Res. Lett.*, *35*, L12505, doi:10.1029/2008GL033365.

Ritz, C., A. Fabre, and A. Letreguilly (1997), Sensitivity of a Greenland ice sheet model to ice flow and ablation parameters: Consequences for the evolution through the last climatic cycle, *Clim. Dyn.*, *13*, 11–24.

Ritz, C., V. Rommelaere, and C. Dumas (2001), Modeling the evolution of Antarctic ice sheet over the last 420,000 years: Implications for altitude changes in the Vostok region, *J. Geophys. Res.*, *106*, 31,943–31,964.

Rommelaere, V., and D. MacAyeal (1997), Large-scale rheology of the Ross Ice Shelf, Antarctica, computed by a control method, *Ann. Glaciol.*, *24*, 43–48.

Schodlok, M., D. Menemenlis, E. Rignot, and M. Studinger (2012), Sensitivity of the ice-shelf/ocean system to the sub-ice-shelf cavity shape measured by NASA IceBridge in Pine Island Glacier, West Antarctica, *Ann. Glaciol.*, *53*(60), 156–162.

Schoof, C. (2007a), Marine ice-sheet dynamics. Part 1. The case of rapid sliding, *J. Fluid Mech.*, *573*, 27–55.

Schoof, C. (2007b), Ice sheet grounding line dynamics: Steady states, stability, and hysteresis, *J. Geophys. Res.*, *112*, F03S28, doi:10.1029/2006JF000664.

Seroussi, H., M. Morlighem, E. Rignot, E. Larour, D. Aubry, H. Ben Dhia, and S. S. Kristensen (2011), Ice flux divergence anomalies on 79north Glacier, Greenland, *Geophys. Res. Lett.*, *38*, L09501, doi:10.1029/2011GL047338.

Shapiro, N., and M. Ritzwoller (2004), Inferring surface heat flux distributions guided by a global seismic model: Particular application to Antarctica, *Earth Planet. Sci. Lett.*, *223*, 213–224.

Studinger M., et al. (2012), Mapping Pine Island Glacier's sub-ice cavity with airborne gravimetry, Abstract C11A-0528 presented at 2010 Fall Meeting, AGU, San Francisco, Calif., 13–17 Dec.

Takeda, A., S. Cox, and A. Payne (2002), Parallel numerical modelling of the Antarctic ice sheet, *Comp. Geosci.*, *28*, 723–734.

Utke, J., U. Naumann, M. Fagan, N. Tallent, M. Strout, P. Heimbach, C. Hill, and C. Wunsch (2008), OpenAD/F: A modular open-source tool for automatic differentiation of Fortran codes, *ACM Trans. Math. Software*, *34*(4), 18, doi:10.1145/1377596.1377598.

van der Veen, C. J., and I. M. Whillans (1989), Force budget: I. Theory and numerical methods, *J. Glaciol.*, *35*, 53–60.

Vaughan, D., et al. (2006), New boundary conditions for the West Antarctic Ice Sheet: Subglacial topography beneath Pine Island Glacier, *Geophys. Res. Lett.*, *33*, L09502, doi:10.1029/2005GL025561.

Vieli, A., A. J. Payne, Z. Du, and A. Shepherd (2006), Numerical modelling and data assimilation of the Larsen B Ice Shelf, Antarctic Peninsula, *Philos. Trans R. Soc. A*, *364*, 1815–1839.